Ultrasonics 56 (2015) 80–89

Contents lists available at ScienceDirect

Ultrasonics

journal homepage: www.elsevier.com/locate/ultras

Towards GHz–THz cavity optomechanics in DBR-based semiconductor resonators

N.D. Lanzillotti-Kimura [a], A. Fainstein [b,*], B. Jusserand [c]

[a] Laboratoire de Photonique et de Nanostructures, C.N.R.S., 91460 Marcoussis, France
[b] Centro Atómico Bariloche & Instituto Balseiro, C.N.E.A., 8400 S.C. de Bariloche, R.N., Argentina
[c] Institut des NanoSciences de Paris, UMR 7588 C.N.R.S., Université Pierre et Marie Curie, 75015 Paris, France

ARTICLE INFO

Article history:
Received 12 February 2014
Received in revised form 28 April 2014
Accepted 23 May 2014
Available online 6 June 2014

Keywords:
Ps acoustics
Coherent phonon generation
Cavity optomechanics
Semiconductor devices

ABSTRACT

Resonators based on acoustic distributed Bragg reflectors (DBRs) were optimized to work in the GHz–THz regime, and grown by molecular beam epitaxy. We show that in structures made of GaAlAs alloys a simultaneous optimal confinement of light in the visible range and phonons in the tens of GHz range can be achieved. We report time resolved differential optical reflectivity experiments performed with fs–ps laser pulses. The experimental results are in excellent agreement with simulations based on standard transfer matrix methods. The resonant behavior of the photoelastic coefficient is discussed. The perfect optic-acoustic mode overlapping, added to a strongly enhanced coupling mechanism, implies that these DBR-based cavities could be the base of highly efficient optomechanical resonators.

1. Introduction

Semiconductor multilayers, mainly based on GaAs and AlAs, have been studied at length for their interesting electronic, vibrational, and optical properties, and for the ability developed to fabricate structures of exceedingly high quality based on molecular beam epitaxy (MBE) techniques. Because of the relatively high acoustic impedance mismatch between the two materials, high-reflectivity acoustic mirrors can be obtained with periodic (SL) structures [1,2]. Aperiodic specifically optimized structures, on the other hand, can be designed to perform as color or notch filters, broadband mirrors, or essentially any other passive acoustic device [3–10]. From the electronic point of view, GaAs/AlAs structures are at the base of the fundamental and applied research on quantum wells (QWs) and multiple quantum wells (MQWs) which have allowed, through quantum confinement, to strongly modify the light-matter interaction. Resonant electronic states can be spatially localized, and spectrally tuned, to tailor the interaction of photons with electrons, and through them also with phonons. In addition, exciton formation due to electron–hole interaction leads to strongly enhanced oscillator strengths. GaAs and AlAs are transparent below 1.42 (1.52) eV at room (low) temperatures, displaying contrasting index of refraction (3.57 and 2.96 respectively). This makes these materials also attractive for the conception of optical mirrors and cavities, a fact that has led to the broad and expanding fields of cavity polaritonics, and low threshold lasers [11–21]. Briefly, GaAs and AlAs are extremely powerful materials of choice for optoelectronic, photonic and phononic applications.

Based on the above considerations, we have introduced the idea of acoustic nanocavities based on distributed Bragg reflectors (DBRs). These resonators could be at the base of phonon lasers, and other active acoustic devices. They can be designed to confine phonons up to THz frequencies with very high Q-factors (long lifetimes), strong spatial and spectral confinement, and essentially perfect coupling to the outside. Acoustic nanocavities have been studied both in the spectral (Raman) [22–25] and temporal (picosecond acoustics and coherent phonon generation) [1,26–30] domains. The photon confinement in optical microcavities has also been exploited to enhance the coupling of light with vibrations, again also in spectral [31–34] and temporal domain [35–37] experiments. Enormously enhanced Raman cross sections (up to 10^8, Ref. [38]) and coherent phonon generation efficiencies (up to 10^6) have been demonstrated [39,40]. In addition, and most interestingly, cavities lead to selection rule modifications that allow and enhance otherwise forbidden processes. More specifically, Raman selection rules are modified in such a way to allow the observation of acoustic nanocavity modes and otherwise non-overlapping generation and detection ps-acoustics bandwidths in SLs and MQWs

* Corresponding author. Tel.: +54 2944445100; fax: +54 2944445299.
E-mail addresses: daniel.kimura@lpn.cnrs.fr (N.D. Lanzillotti-Kimura), afains@cab.cnea.gov.ar (A. Fainstein).

http://dx.doi.org/10.1016/j.ultras.2014.05.017
0041-624X/

become perfectly matched [37,40]. This direct excitation of vibrations in the microcavity is related to other strategies oriented to the modulation of the optical properties of microcavities through phonon pulses or surface acoustic waves [35,39,41–50].

A natural question thus emerges: will a resonator designed for optimal optical confinement (i.e., a photon microcavity), perform satisfactorily at the same time as an acoustic resonator (i.e., a phonon cavity) [23,51–60]? This question is critical for the potential use of DBR based cavities as optomechanical resonators. As we have recently demonstrated, the answer is positive [61]. Indeed, a "double magic coincidence" exists both for the acoustic and refractive index ratios, and for the sound and light speed ratios in GaAs/AlAs materials, such that structures turn out to be *optimally* designed to perform *both* as acoustic and light resonators, confining photons and phonons precisely at the same spatial location. The consequence is the conception of novel cavity optomechanical devices that, as we show, display perfect light-sound mode overlap, high vibrational frequencies (20–100 GHz range), huge optomechanical coupling (in the THz/nm range), perfect phonon extraction, potentially low effective mass in pillar structures, and consequently potentially very low phonon lasing thresholds [28,62–66]. An interesting feature of these materials, as compared to others used in cavity optomechanics (specifically Si and SiO_2), is the presence of a resonant photoelastic coupling mechanism, in addition to the more standard purely "mechanical" mechanisms (radiation-pressure or interface-displacement) and the possibility to combine optomechanics and optoelectronics phenomena in the same device [67].

In this contribution we will review the development of these GaAs/AlAs DBR-based optomechanical resonators, emphasizing recent results and discussing in detail the microscopic mechanisms involved. After introducing acoustic nanocavities in Section 2 and discussing the possibility to selectively excite confined vibrations in these structures in Section 3, we present optical microcavities in Section 4 as a means to strongly amplify the photon-phonon interaction in coherent phonon generation experiments. These concepts lead to the conception of DBR-based GaAs/AlAs optomechanical resonators which are described in Section 5. These resonators add to the standard "mechanical" (laser pressure or interface displacement) mechanisms, the possibility to strongly enhance the light-matter interaction through a resonant photoelastic process. The latter is analyzed in detail in Section 6 after which conclusions and prospects for future work are presented.

2. Acoustic nanocavities

Following the example of one-dimensional photonic crystals, in which the electromagnetic field distribution is artificially modified in one dimension by spatially modulating the refractive index, the concepts of one-dimensional phononic crystals and cavities have been introduced for the manipulation of acoustic phonons. In the case of acoustic phonon devices, the relevant parameter determining the reflection and transmission coefficients at each interface are the speed of sound and mass density of the materials.

The simplest phononic device is a periodic structure, where the unit cell is formed by two layers of different materials, i.e., a superlattice. In a bulk material, we can consider that the dispersion relation of the acoustic phonons is linear. The modulation of the acoustic properties introduced by the superlattice is the origin of the folding of the acoustic dispersion relation, defining a new Brillouin mini-zone determined by the thickness of the unit cell. Depending on the thickness ratio of the two layers (and the corresponding material speeds of sound), minigaps will open at the center and edge of the new Brillouin zone. The acoustic wavelength $\lambda_{ac} = v/f$ in each material results the relevant design parameter, where v is the speed of sound and f the target frequency. As an example, a $(\lambda_{ac}/4, \lambda_{ac}/4)$ SL of GaAs/AlAs will optimize the minigaps at the zone edge, while a $(3\lambda_{ac}/4, \lambda_{ac}/4)$ will present optimized minigaps in the zone center. These minigaps are energy bands were no real wavevectors are defined, thus no energy transport can take place. In a finite size sample, this can be observed as the constructive (destructive) interference generated by the multiple interfaces in a reflection (transmission) experiment. The bandwidth of the high reflectivity regions is determined by the contrast of the acoustic impedance of the used materials, while the maximum reflectivity is also determined by the number of periods. As such, a superlattice works with acoustic waves in the same way an optical distributed Bragg reflector (DBR) works for light. The effective thickness of the layers will fix the working wavelength of the mirror [2,22,31].

A planar acoustic cavity is conceptually similar to a Fabry–Perot resonator in which two high-reflectivity mirrors are separated by a spacer. The metallic reflectors are replaced by acoustic DBRs. The resonant condition is achieved when the spacer thickness matches an integer number n of half-wavelengths ($n\lambda_{ac}/2$). In order to achieve GHz–THz frequencies thicknesses of the order of 1–100 nm are necessary. Since the performance of the mirrors depends on an interference phenomenon, the quality of the interfaces (roughness) and the thickness indetermination should be much smaller than the working acoustic wavelength. These requirements are nowadays achievable by means of molecular beam epitaxy [22,23,25].

The efficient generation and detection of these high frequency phonons are one of the main challenges in nanophononics. In contrast with acoustics and phononics where piezoelectric transducers are available, the transduction of sub-THz acoustic nanowaves relies mainly on ultrafast optical methods [1,29,44,45,65,68–80]. By the same token, the coupling between vibrations and light is the very backbone in optomechanics. Coherent phonon generation, picosecond ultrasonics and pump–probe in nanophononics usually refers to the set of generation, control and detection techniques of coherent acoustic phonons using ultrafast lasers.

In the basic pump–probe experiment a pulsed ultrafast laser is divided into two different paths: an intense beam, the pump; and a weak beam, the probe. The probe beam is delayed using a mechanical delay line. In order to allow a synchronous detection, the pump beam is modulated at MHz frequencies using an acousto-optic modulator. Both beams are then focalized onto the sample typically using a single lens. The reflected signal from the probe is detected using a photodiode and processed using a lock-in amplifier. The physical process that takes place can be described as follows: (i) a pump pulse excites a phonon population (a mechanical strain generated by a thermoelastic, electrostriction or deformation potential mechanism), (ii) these phonons modulate the refractive index of the materials forming the structure; and (iii) the probe pulse senses the variations in reflectivity induced by the coherent phonons at a given delay. This process is repeated for different delay times, allowing to reproduce the time dependent reflectivity curve of the sample.

In a simplified model, the coherent phonon generation can be described as follows [29]:

$$g(\omega) = \alpha \int \kappa(z)\eta_0(\omega, z)|E_p(z)|^2 dz. \quad (1)$$

And the detection selection rules can be condensed in the following expression:

$$\Delta r = \beta \left\{ \int p(z)\eta(\omega, z)E_0^2(z)dz + \sum_{m=0}^{2N} (\epsilon_{m-1} - \epsilon_m)u(z_m)(a_m + b_m)^2 \right\}. \quad (2)$$

In Eqs. (1) and (2), α and β are proportionality constants, η_0 the elastic strain eigenstates, η is the elastic strain in the sample, E the electric field inside the sample, κ is an effective generation constant that considers different light-matter couplings, p the photoelastic constant, and g and Δr are the amplitude of the generated phonons and the reflectivity change respectively. In Eq. (2), ϵ_m is the dielectric function of layer m, and z_m is the position of the interface between layers m and $m+1$. The probe field within layer m is $E_0(z) = a_m e^{i\sqrt{\epsilon_m}kz} + b_m e^{-i\sqrt{\epsilon_m}kz}$, and $\sqrt{\epsilon}k$ is the light wavevector. The first term in Eq. (2) is due purely to the photoelastic effect (i.e., a change in the index of refraction). The second results from the displacement of the interfaces (i.e., an effective change in the thickness distribution of the cavity). The latter is fully determined by a proper evaluation of the acoustic modes of the structure, and by physical constants (dielectric functions) that are readily available for most materials. The photoelastic term in Eq. (2), on the other hand, is proportional to the photoelastic constant p that has only been measured for a few materials, and even in those cases for a limited range of wavelengths. This problem will be addressed in Section 6 below.

Looking at these expressions it is clear that it is possible to change the efficiency of each one of the processes and to change the efficiency of the whole generation–detection process by engineering the materials selection (affecting the generation and photoelastic constants), the electric field distribution and the strain eigenstates. In standard optomechanics the excitation laser is far from electronic resonances, and thus the interface displacements tends to be more important. Optoelectronic semiconductors open the possibility of using an extra engineering parameter: the resonance of the photoelastic term. In the remaining of this paper we will discuss how to tailor these processes using (i) electronic resonances, (ii) optical confinement, and (iii) mechanical resonances, targeting a structure where a perfect overlap between the electric and displacement fields is achieved and the interactions strongly enhanced.

The top panel of Fig. 1 shows the time resolved reflectivity curve measured on a GaAs/AlAs superlattice. This superlattice has been optimized to present the first minigap at the Brillouin zone center at around 1 THz. The sharp peak observed at $t = 0$ ps corresponds to the electronic excitation of the sample, while the slow variation of the signal for $t > 0$ ps is related to a temperature change and electron–hole recombination dynamics in the system. In the inset we show a detail of the time resolved reflectivity between 50 and 100 ps. In this range it is possible to observe high frequency oscillations induced by coherent phonons. Two periods can be easily identified: oscillations of approximately 1 ps period are mounted on a 20 ps period oscillation.

The bottom panel of Fig. 1 shows the Fourier transform of the signal show in the top panel. For clarity reasons the slow dynamics-related background has been removed from the signal, and the electronic signal omitted from the window on which the FT is performed. A group of three peaks are clearly observed around 1 THz. The peaks labeled with red circles are related to $q = 2k$ condition, where q is the acoustic wavevector, and k is the laser wavevector. This is the condition under which the detection is most efficient [29]. The peak indicated with a blue square is related to the $q = 0$ phonons, where the generation process results most efficient [29]. These selection rules are strict only for infinite samples. In fact, generation and detection spectral overlap becomes possible when finite size or absorption are present [29]. The peak at around 50 GHz is the so-called Brillouin mode, and corresponds to the first intersection of the $q = 2k$ line with a linearized acoustic dispersion relation (see the inset in Fig. 1b). The relative intensity of these peaks is strongly related to the aforementioned selection rules that are derived from the matching between the electric and strain fields.

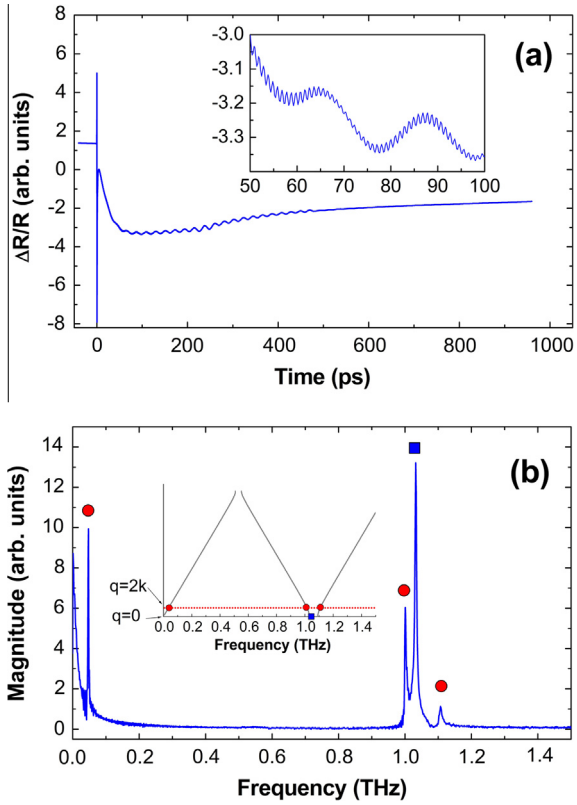

Fig. 1. Panel a: Time resolved reflectivity measured on a GaAs/AlAs superlattice. The sharp peak at $t = 0$ ps corresponds to the electronic excitation of the sample, while the slow variations related to the temperature change and electron–hole recombination dynamics in the system. A zoom of the time resolved reflectivity between 50 and 100 ps is shown in the inset. The high frequency oscillations are induced by high frequency coherent acoustic phonons. Panel b: Magnitude of the FT of the time-resolved pump–probe reflectivity experiment. The peaks indicated with circles correspond to the $q = 2k$ condition, while the peak indicated with a square is related to the $q = 0$ condition. The inset illustrates the folded dispersion relation of the acoustic phonons.

One of the desirable tasks is to spectrally select the frequency of the acoustic phonons that are excited and detected. As we show next, this can be accomplished by means of (i) time domain coherent control, (ii) the spatial overlap of the electric and mechanical fields, and (iii) using electronic resonances in the structure that locally enhance the transduction by tuning the laser energy.

3. Selective generation of confined acoustic modes

Achieving a monochromatic source of high-frequency coherent phonons is a main challenge in the search of an acoustic lasing device (SASER). Based on the characteristics of the semiconductor structures, there are at least three possible approaches to reach the selectivity in the excitation of a quasi monochromatic phononic mode in a pump–probe experiment:

- Coherent excitation by temporal modulation of the excitation [79–87]. In other words, by performing a coherent control experiment using multiple excitation pulses and controlling time profile it is possible to resonantly excite one of the acoustic modes, annihilate others, manipulate the intensity distribution, and in a general way to synthesize a phononic pulse. This technique has been used in the past both in semiconductor multilayers, metallic nanostructures, and nanoparticles to excite particular modes [79–87]. In Fig. 2 we show how a phonon nanocavity mode can be manipulated using pairs of pump

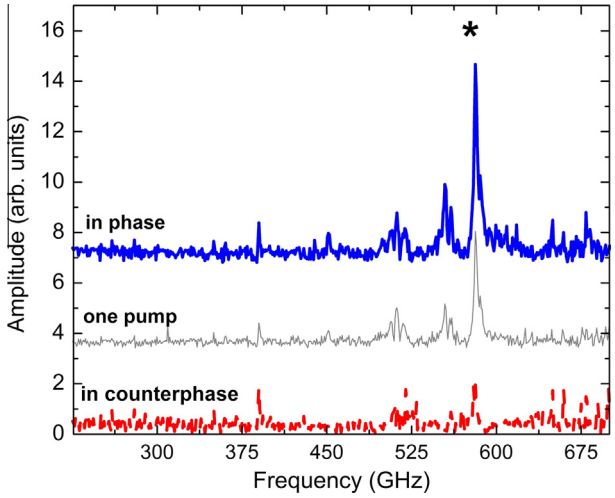

Fig. 2. Acoustic nanocavity spectra measured in the coherent control scheme with two pump pulses in-phase (top, continuous line), two pump pulses in counterphase (bottom, dashed line), and with one pump pulse (middle, gray thin line). The star indicates the acoustic cavity mode peak.

pulses and varying the separation between them [36]. To perform this experiment two pump lasers where used with a time delay that matches one half and one full period of the confined phonons. The grey line in Fig. 2 corresponds to a single pump inciding on the sample.

- Resonant excitation with an electronic level in a semiconductor nanostructure. Due to confinement effects, layers with different thickness in the nm-range, will have associated different electronic transitions. Thus it is possible to perform an engineering of the involved layer thickness and material composition in order to have a spatially localized absorption of light, and consequently a localized generation of mechanical strain [73,88]. By tuning the pump pulse energy to the cavity spacer electronic transition it is then possible to selectively excite the confined acoustic mode [88]. As we will discuss later, the photoelastic constants present strong variations around electronic resonances, affecting also the detection efficiency of monochromatic signals.
- Spatial selectivity of the excitation, i.e., to localize the electrical field in a particular region of space in order to excite (or detect) more efficiently a given acoustic mode by matching the desire strain profile. The dimensions involved in the nanocavities we presented up to now are much smaller than the optical wavelengths in the Vis–NIR bands. Thus this strategy cannot be directly applied in the sub-THz regime as in the photoacoustic study of microscopic objects. As we will show below, the technique is readily applicable in the 10–100 GHz range.

Taking into account these strategies, the next sections explore how the engineering of the electric fields, and the spatial matching between the electromagnetic and strain fields can enhance the generation and detection of monochromatic coherent acoustic phonons.

4. Enhancement of pump–probe signals using microcavities

One way to modify the electric field distribution in a pump–probe experiment is to generate a stationary spatially localized wave using a planar optical microcavity. Optical distributed Bragg reflectors (DBRs) are constructed by growing periodic sequences of bilayers of materials of contrasting index of refraction, n. The refractive index mismatch ($Z_{op} = n_1/n_2$), and the number of bilayers (N) determine the performance of a mirror. For a given Z_{op} and N, the optimal mirror (i.e., with the largest forbidden optical gap, and the highest reflectivity) is obtained by choosing $(\lambda_1/4, \lambda_2/4)$ stacks, where λ_l is the optical wavelength in material l. Since this latter wavelength depends on the index of refraction, it is Z_{op} that determines the optimal relation of thicknesses between the two materials. A DBR-based optical cavity is obtained by growing two DBRs enclosing a spacer. The optimal spacer thickness corresponds to an integer number m of half-wavelengths, $d_{cav} = m\lambda_l/2$. Note that this structure resembles the previously discussed acoustic nanocavities. For an optical wavelength of 800 nm, the typical period is ~120 nm while for an acoustic nanocavity in the THz range as discussed above the period is ~8 nm.

The confinement of the electric field has two main consequences: on one hand it locally enhances the electric field, and thus the efficiency of the generation and detection processes; on the other hand, the spatial modulation modifies the spectrum of the detectable phonons, and as a result the generated spectrum perfectly matches the detected spectrum [40]. By the same token, this spatial modulation implies also a spatially modulated strain generation. It has previously shown that the condition to maximize the generation efficiency is to tune the pump wavelength to the optical cavity mode; while the condition to maximize the detection sensibility is to tune the laser wavelength with the edge of the optical cavity mode [37,39,40]. Using a single laser, i.e. a single wavelength, it is possible to achieve both conditions simultaneously taking advantage of the angular dispersion of the optical cavity mode by adjusting the incidence angles according to:

$$\omega(k_{||}) = \sqrt{\omega_0^2 + (ck_{||}/n_{eff})^2}, \tag{3}$$

where c and n_{eff} are the speed of light and the index of refraction of the microcavity spacer, respectively. In the case studied in this section, an acoustic nanocavity is enclosed between two optical DBRs in such a way that it acts as the optical spacer of an optical cavity. Provided that the layers forming the acoustic nanocavity are much smaller than the optical wavelength, an effective index of refraction should be considered weighting the contributions of the different materials forming the acoustic structure.

Fig. 3a shows a schematics of an acoustic cavity structure embedded in an optical microcavity. The top (bottom) mirror of the studied microcavity is a 3(10) periods $Ga_{0.8}Al_{0.8}As$/AlAs 55.39/64.19 nm, corresponding to a $(\lambda_l/4, \lambda_l/4)$ stack. The full acoustic nanocavity structure acts as a $2\lambda_l$ spacer. Each acoustic DBR is formed by 13 bilayers of (GaAs/AlAs) 5.75/2.27 nm, corresponding to a $(3\lambda_{ac}/4, \lambda_{ac}/4)$ stack; while the acoustic spacer is a $3\lambda_{ac}/2$ GaAs layer. It is worth highlighting that in this structure $\lambda_{ac} \ll \lambda_l$.

In Fig. 3c we show the amplitude of the measured acoustic nanocavity mode as a function of laser wavelength (keeping the incident angles constant). There is a clear maximum around 760 nm. This maximum corresponds to the optimum coupling of the pump laser with the cavity mode and the maximum sensitivity of the probe tuned to the edge of the cavity mode at the incidence angle chosen. This coupling condition was achieved by setting the pump beam at almost normal incidence and the probe at ~30° degrees (see Fig. 3b). In the top panel of Fig. 3c we present the reflectivity measured directly with the pulsed laser for both angles. The curve in grey corresponds to the derivative of the reflectivity of the probe beam. The second maximum at 747 nm corresponds to an additional point where a balance between an optimized detection efficiency (minimum in the derivative) and maximal generation efficiency are attained. Similar double resonant schemes using microcavities were previously reported in Raman spectroscopy [37,40].

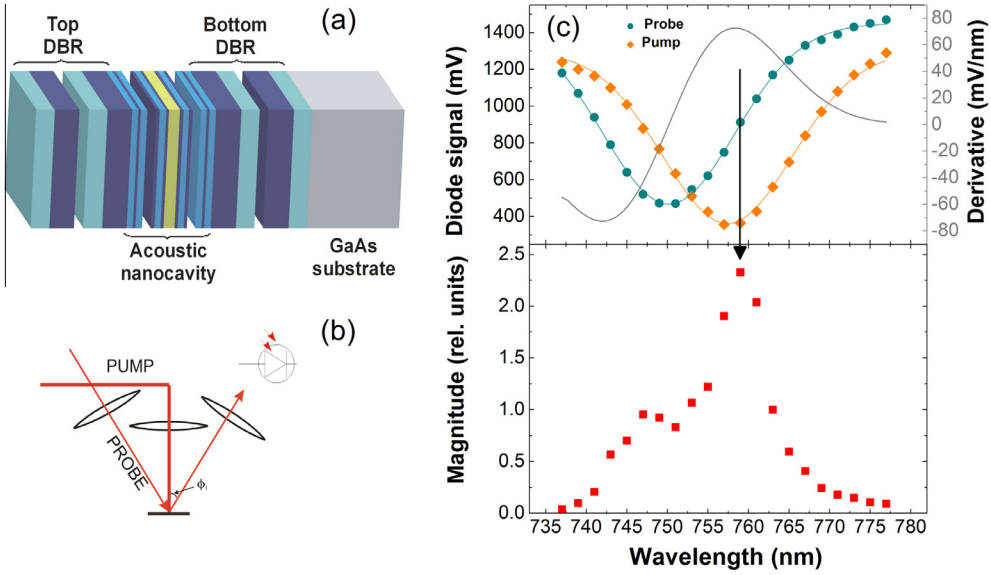

Fig. 3. (a) Schematics of an acoustic cavity structure embedded in a optical microcavity. (b) Experimental configuration to perform a double optical enhanced pump–probe experiment taking advantage of the microcavity angular dispersion. (c) Coherent acoustic phonon generation. Top panel: optical reflectivity curve measured with the diode for both the pump and probe beams. The thin curve corresponds to the numerical derivative of the probe reflectivity. The lower panel shows the acoustic cavity mode amplitude as a function of the laser wavelength. The arrow indicate the position of the microcavity mode center.

The next section is devoted to the study of the particular case where $\lambda_{ac} = \lambda_l$. That is, the thickness of the layers making the acoustic nanocavity (THz frequencies, nm-size thicknesses) are augmented, keeping the same optimized ratio, until the structure acquires dimensions characteristic of optical microcavities (periods in the range of 100 nm). Moreover, λ_l will be selected such that the photon cavity energy is close to the electronic resonance of the cavity spacer allowing for a spatially selective excitation, as discussed above [88].

5. Simultaneous resonators for light and sound

The fundamental structure and design of an acoustic nanocavity and an optical microcavity are based on the same concept: a Fabry–Perot resonator where the metallic mirrors are replaced by distributed Bragg reflectors. The design parameter in the acoustic case are the sound velocity and the mass density while in the case of the optical microcavities is the index of refraction.

A structure formed by 20(18) periods of AlAs/$Ga_{0.82}Al_{0.18}As$ $(\lambda_l/4, \lambda_l/4)$ bilayers for the top (bottom) mirror enclosing a $\lambda/2$ GaAs layer is an optimized optical microcavity with the first confined mode centered at a wavelength of 870 nm [89]. Taking into account the previous discussion, we ask ourselves how does the same structure perform as an acoustic cavity for longitudinal acoustic phonons of the same wavelength. "Optimal" implies that the cavity mode (either acoustic or optical) falls at the center of a DBR stop band, and the Q-factor is the largest for the materials chosen [90]. The key and new concept here is that for GaAs and AlAs (and any alloy made of these materials) a "double magic" coincidence exists: (1) the ratios of (light and sound) velocities are almost identical and (2) the (light and sound) impedance contrasts are also almost identical. This implies that the same optical microcavity optimized to confine photons will optimally confine acoustic phonons of the same wavelength and with the same Q factor [61]. As it can be seen in Fig. 4, in this structure there is a perfect matching between the electric and atomic displacement fields. In this case the fundamental cavity confined acoustic mode falls around 20 GHz. Typically, DBR semiconductor cavities have Q-factors in the range 10^3–10^5, depending on the number of periods forming the DBR.

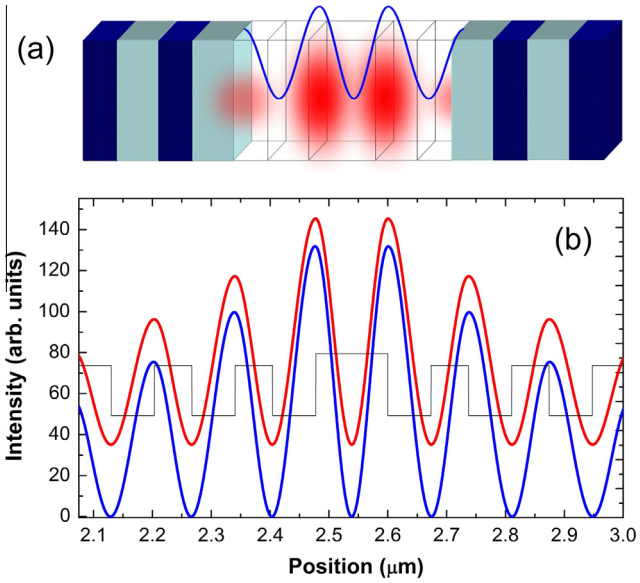

Fig. 4. (a) Schematics of an acoustic cavity structure optimized to work at the 20 GHz frequency range. The cavity spacer is made of GaAs while the DBRs are based on AlGaAs alloys. The structure is able to simultaneously confine photons in the visible-near infrared range and phonons in the GHz–THz range. (b) Detail of the calculated optical (red) and acoustic displacement (blue) fields for fundamental cavity modes. The curves have been vertically displaced for clarity reasons. Note the perfect matching between both fields. (For interpretation of the references to color in this figure legend, the reader is referred to the web version of this article.)

The performance of the optical cavity structure can be easily tested by means of a photoluminescence (PL) experiment using an excitation laser of 647 nm. In Fig. 5a we show the PL spectra taken at room temperature on two different points on the sample. The studied structure was grown with a gradient in the thickness in such a way that the wavelength of the optical mode depends on the position on the sample where the experiment is performed. The two cases shown correspond to the cavity mode tuned to the transparency region below the gap (881 nm) and precisely tuned at the gap (870 nm), respectively. From the measured spectrum a

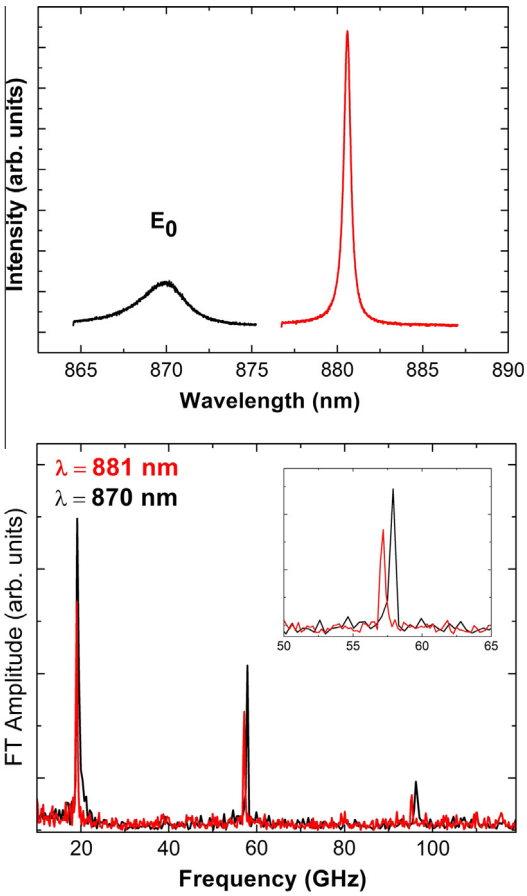

Fig. 5. Top: Photoluminescence measured at room temperature for two different positions on the sample, i.e. cavity-bandgap detunings (the structure was grown with a gradient in thickness). E_0 indicates the position of the GaAs bandgap. Bottom: Pump probe signal measured with the laser near the bandgap of the GaAs (cavity spacer), and below the bandgap. The three peaks correspond to the three first confined modes at the Brillouin zone edge. The inset shows a detail of the mode around 60 GHz. Note the clear shift for the two different spot positions (i.e., cavity thicknesses).

quality factor (Q-factor) of $\sim 10^3$ can be derived for this sample when measured below the gap.

In order to probe the elastic behavior of the resonator we performed coherent phonon generation experiments on the structure using 1 ps laser pulses, tuned approximately with the cavity mode. The FWHM of the optical cavity mode is ~1 nm, so the temporal width of the laser pulse must be adjusted to match the finesse of the resonator. In the bottom panel of Fig. 5 we show typical spectra obtained with this technique. The peaks observed at ~20, ~60, and ~100 GHz correspond to the first three cavity confined acoustic modes. It is worth highlighting as shown in Fig. 5 that different positions on the sample give not only different optical cavity mode energies, but also different acoustic cavity mode frequencies, thus demonstrating the simultaneous confinement of light and hypersound. For the two measured spectra note that the larger optical Q-factor-resulting in an enhanced signal-compensates the reduced absorption at longer wavelengths leading to similar picosecond acoustics signal intensities. The measured time traces were 3 ns long, thus limiting the intrinsec bandwidth resolution and quality factor measurement of the acoustic system. The nominal mechanical Q-factor is of the order of 1000 as in the case of the electromagnetic counterpart, and the estimated acoustic cavity mode lifetime is about 30 ns.

The top panel of Fig. 6 shows the optical reflectivity obtained using the ~1 ps probe laser pulses. The full curve is the numerical derivative of the probe reflectivity. The central panel presents the coherent phonon (amplitude of the peaks shown in Fig. 5) peak intensity as a function of the position on the sample, directly related to the laser-cavity detuning. The bottom panel presents the electronic signal amplitude (amplitude of the time trace at $t = 0$ ps) as a function of the position on the sample. Note that the maxima of both vibrational and electronic signals are observed when the probe is tuned to the edge of the cavity mode [40]. This demonstrates unambiguously that the observed oscillations are due to the modulation of the cavity reflectivity by phonons belonging to the resonator.

In picosecond ultrasonics experiments the information of the acoustic phonon dynamics is readily available. A color map displaying the experimental windowed Fourier transforms (WFTs) amplitude as a function of time-delay is shown in Fig. 7(a and b). The reported WFTs were obtained by calculating the Fourier transform of the derivative of the measured time-traces (to reduce the contribution of the slowly varying electronic signals), in time windows of 500 ps width. The center of these windows was continuously varied between 250 and 2750 ps to extract the time dependence of the phonon mode population. The data were convoluted with Gaussians of width $2\sigma = 250$ ps centered within the 500 ps window ("Gaussian window Fourier transforms"). Similar results were obtained using other functions (e.g., Hann window). The results with simple square windows lead to essentially the same results, albeit with some unphysical weak high frequency oscillations originated in the window boundaries. The width of the windows was chosen as a compromise for having the required time resolution, without loosing relevant spectral information. We have verified, however, that the main conclusions of the paper do not depend on the chosen parameters. Strong oscillations and a rich behavior are observed for the mode amplitudes as time evolves. A peculiar event occurs around 900 ps, characterized by a strong dip of the 20 GHz mode intensity, a "shake-up" of the 60 GHz mode, and the appearance of additional frequencies in the spectra.

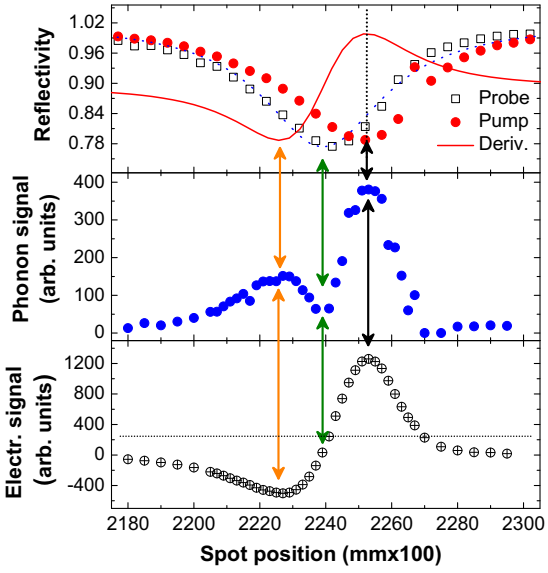

Fig. 6. Top panel: optical reflectivity obtained using the probe laser pulses set at $\lambda_{op} = 870$ nm. The full curve is the numerical derivative of the probe reflectivity. Middle: coherent phonon peak intensity. Both panels are given as a function of the position of the spot on the sample, directly related to the detuning between the laser wavelength and the cavity mode at normal incidence. Bottom: Amplitude of the detected electronic signal (time trace a $t = 0$ ps). Note how the electronic signal follows the behavior of the derivative of the probe reflectivity. The phonon signal intensity is approximately the modulus of the latter.

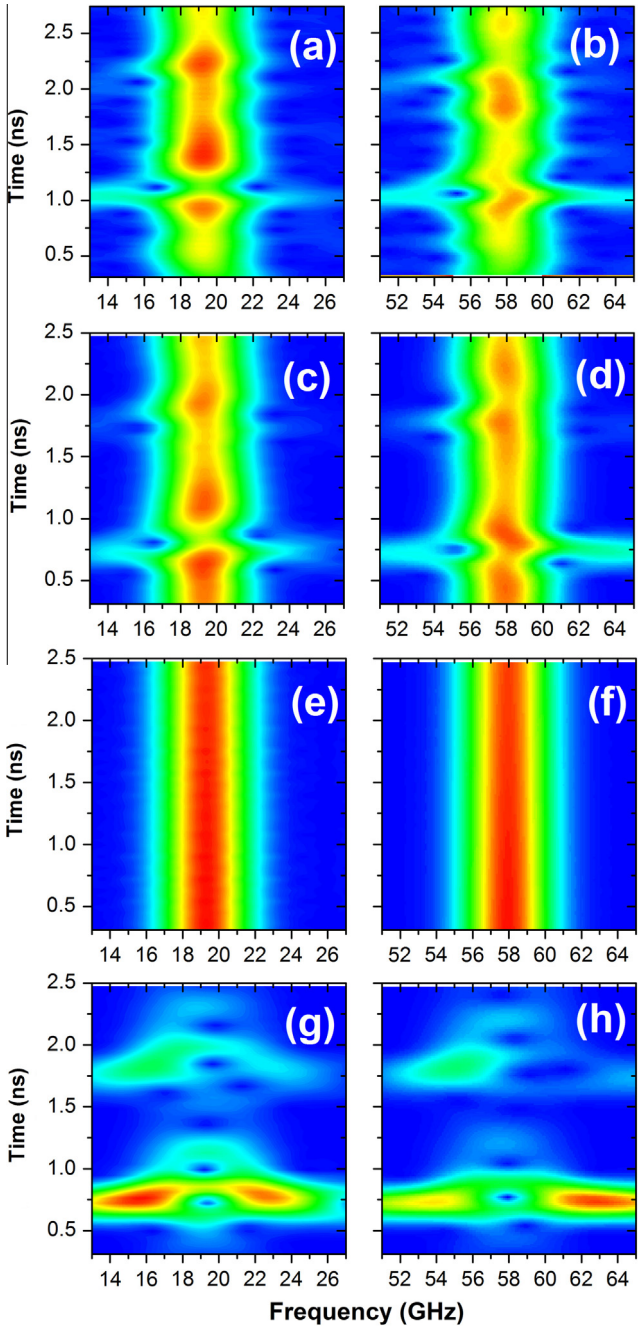

Fig. 7. (a and b): Detail of the experimental WFT intensity map corresponding to the 20 (a) and 60 (b) GHz cavity modes. The separate color intensity scale has been chosen to emphasize the relative variation of the corresponding phonon signal. Note the intensity beatings displayed between the two acoustic phonon modes. See the text for further details. (c–h): Calculated WFT intensity maps for the same spectral regions. Six panels are shown corresponding to the WFTs obtained from the full calculation (c and d), from the time trace obtained by spectrally filtering the cavity modes only (e and f), and from the time trace with all modes *except* the cavity modes (g and h).

Panels (c and d) in Fig. 7 display the WFT of the calculated differential reflectivity time traces obtained using Eqs. (1) and (2). Except for the overall amplitude, no fitting parameters are used, only nominal thicknesses and published material properties data were included. The agreement between experiment and theory is quite notable, with the most relevant features being nicely reproduced: the intensity oscillation of the modes, and the effects due to the echo "shock" at ~900 ps. From the calculations it becomes clear that these peculiar features originate in the strong perturbation produced by an echo of the initial phonon pulse generated at the GaAs spacer, that propagates to and is reflected by the sample surface.

To further clarify how this occurs, we show in Fig. 7(e–h) the WFTs of the calculated differential reflectivity time trace due *exclusively* to the cavity modes (e-f), and the equivalent trace corresponding to all modes *other than* the cavity modes (g–h). The pure cavity modes display a slowly decaying monotonic behavior, as expected for a confined vibration. The non-confined components, on the other hand, escape the GaAs spacer very rapidly, within the first ~20 ps, and are echoed back to the GaAs-spacer at ~900 ps.

The excellent agreement between experiment and theory suggests that this model can be used to evaluate the performance of the structure as an optomechanical resonant device. While this is qualitatively true, coming back to Eq. (2) we recall that for a quantitative description an important level of uncertainty is introduced by the lack of available data for the photoelastic coefficient, the critical parameter required to define the resonant contribution to the optomechanical coupling. As we argue next, this parameter can lead to huge contributions, but has only been determined for a few materials, for only limited laser energy ranges, and, to the best of our knowledge, never in the context of quantum confined electronic transitions.

6. Photoelastic coefficients in Gallium Arsenide based resonators

To take full advantage of the electronic-resonant excitation in semiconductors it is essential to know the photoelastic behavior of the materials involved in the design of the optomechanical resonators. In what follow we briefly discuss the photoelastic characteristics of GaAs in the Vis–NIR range.

Deformation potential is a very important mechanism for the interaction between acoustic strain and optical properties in semiconductors. In usual experimental conditions where the laser energy is close to excitonic transitions, it becomes the dominant mechanism and overcomes the contribution due to interface or surface displacements [61]. A quantitative description of this interaction is therefore of great interest and accurate measurements of the photoelastic coefficient which governs the amplitude of the mechanism as a function of the energy around excitonic resonances is highly desirable. Resonant Brillouin scattering has been applied since a long time to the demonstration of excitonic resonances in the acoustic phonon scattering spectra [91]. However absolute measurements of Brillouin scattering efficiencies remain difficult, and in addition the scattering amplitude reflects only the *absolute* value of the coefficient. The later point is a strong limitation of the method as photoelastic coefficients are predicted to display strong variations of both their real and imaginary parts close to resonance. Independent knowledge of both variations would thus be essential to analyze coherent acoustic and optomechanical experiments close to excitonic resonances.

We have recently demonstrated a huge increase of the light scattering amplitude by acoustic vibrations at the excitonic resonance in a GaAs/AlAs multi-quantum well [92], which points to a very large enhancement of the photoelastic coefficient in these conditions. We cannot deduce from our experiments whether variations of the real or the imaginary part of the photoelastic coefficients play a dominant role in this resonance, but we unambiguously demonstrated that acousto-optic coupling becomes huge in such conditions. In fact, we recently studied as a follow-up of Ref. [92], the variation of the Brillouin forward scattering intensity starting from the strong excitonic resonance and decreasing the

laser energy towards the transparency region where independent measurements of photoelastic constants are available (see below). We observed such a steep decrease of the scattering intensity that the Brillouin lines could not be observed on the low-energy edge of the excitonic resonance as they disappear within the strong persisting luminescence background. However for even smaller energies we recovered the Brillouin lines and could thus obtain an estimation of the global increase by a factor of $(1.5 \pm 0.5)\ 10^5$ of the photoelastic coupling due to excitonic resonance when the laser is changed from 1.485 to 1.521 eV. These results are illustrated in Fig. 8, where the spectra obtained at liquid nitrogen temperature well below (left red curve) and on the exciton (right black curve) are plotted together. For the red curve, the laser line, strongly attenuated by a foremonochromator, is recorded with a similar intensity to the Brillouin lines appearing as a triplet typical to forward scattering configuration [91]. In strong resonance, the Brillouin lines sit on a strong background of resonant luminescence but the intensity can be determined with a reasonable accuracy. Since the Brillouin scattering efficiency is proportional to the square of the photoelastic constant, we deduce an increase by 400 of the modulus of this coefficient when the laser is varied from −36 MeV to zero detuning with the exciton resonance.

This result highlights the relevance to perform other type of experiments to measure the photoelastic coefficient, and not only its modulus, in a large range of energies. Different methods have been reported in the literature and applied to bulk semiconductors: piezobirefringence [93], acousto-optic deflection [94] and piezo-ellipsometry [95]. These techniques apply to complementary situations: piezobirefringence and acousto-optic deflection to transparent samples, and piezo-ellipsometry to energy ranges where absorption is sufficiently large. Piezo-ellipsometry has been mostly applied to the study of higher optical transitions in bulk semiconductors where the large absorption make the technique very sensitive. The technique seems to be not well adapted to low energy excitonic transitions and to the quantum wells as involved in several coherent acoustic and optomechanical applications. Piezobirefringence and acousto-optic deflection give consistent evidences that the real part of the photoelastic coefficient displays a large dispersion when the band gap is approached from the lower energy side, in a range where the imaginary part is negligible. However strong absorption in the thick samples used in these experiments lets the determination closer to the exciton resonance inaccessible.

There are some additional complications in the use of data reported in the literature for GaAs as the definitions of the photoelastic coefficients are varying from paper to paper. For instance, Feldman and Horowitz [93] is using the historical definition: $\mathrm{d}(\epsilon^{-1}) = PX$ while Renosi and Sapriel [94] use: $\mathrm{d}(\epsilon^{-1}) = PU$. On the other hand, Etchegoin [95] presents several curves based on again another definition: $\mathrm{d}(\epsilon) = PX$, while Popovic et al. [96] gives often cited numerical values based on Etchegoin results but changing to the alternative definition: $\mathrm{d}(\epsilon) = PU$. Finally in the context of optomechanics and in the interpretation of pump–probe experiments, the refractive index is many times used in place of the dielectric constant with the following expression: $dn = PU$. In these expressions, U and X are the strain and stress tensors, respectively, P is the photoelastic coefficient, n is the refractive index, and ϵ is the dielectric constant. Knowledge of the elastic and dielectric constant of the materials, allows however to transform from one definition to another and to compare different determinations when the energy range of experiments overlap (keeping in mind that $\mathrm{d}(\epsilon^{-1}) = (-1/\epsilon^2)\mathrm{d}\epsilon = (-2/n^3)\ \mathrm{dn}$). Fig. 9 shows data for the component p_{12} of P of bulk GaAs, extracted from Ref. [94] and obtained at room temperature and converted to the definition used by Popovic and coworkers ($\mathrm{d}\ (\epsilon) = PU$). We checked that these values agree well with determinations by Feldman and Horowitz [93] based on another technique. The coefficient p_{12} is the relevant component involved in our Brillouin and coherent phonon experiments (both detected signals are proportional to $|p_{12}|^2$). It is however not straightforward to directly compare these data with our observation in GaAs MQWs and in strong resonance. After correction from the temperature induced shift of the exciton resonance, and in account of the 400 amplification of the Brillouin scattering efficiency shown in Fig. 8, we deduce that the modulus of the photoelastic constant at the top of the exciton resonance is likely to reach a huge value of the order of 7000 over a narrow range of energies.

Extension of this technique to multilayers seems not to have been reported but could become possible provided that sufficiently transparent samples can be studied. Multi quantum wells with a limited number of wells, designed for an optimum transmission can be easily obtained but the application of uniaxial stress to such

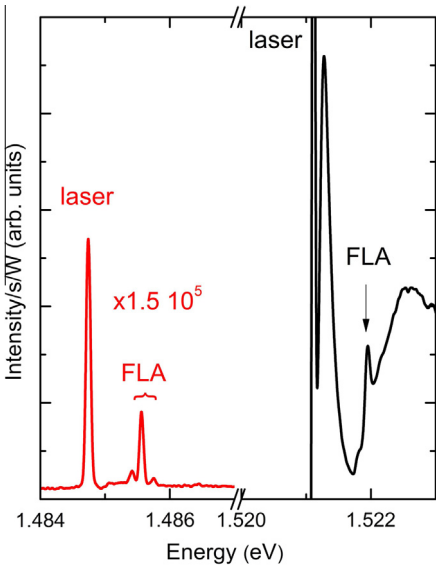

Fig. 8. Experimental Brillouin scattering spectra taken at liquid nitrogen temperature with an excitation laser energy below the gap (left red spectrum) and on the gap (right black spectrum). FLA labels the superlattice folded acoustic phonons. (For interpretation of the references to color in this figure legend, the reader is referred to the web version of this article.)

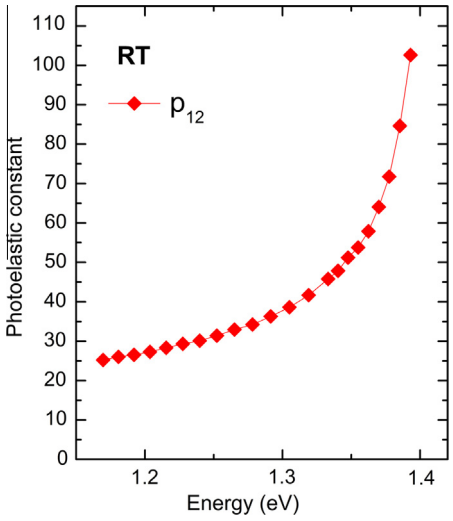

Fig. 9. p_{12} component of the photoelastic tensor as a function of the laser energy, derived from Ref. [94].

structures remains a technical challenge, particularly for the standard GaAs/AlAs structures grown on GaAs substrate as GaAs is opaque at the energies of interest for the quantum well, and thus structures without substrate have to be considered. Waveguided geometries could also be used to study the birefringence under uniaxial stress, but its practical implementation also remains difficult [97]. A more recent technique could help to solve some of the above mentioned issue: reflectance anisotropy spectroscopy [98]. The latter technique has been applied to multiple quantum well structures under uniaxial stress [99] in order to determine intrinsic anisotropies due to interfaces or doping but the quality of the spectroscopic features seems to be compatible with accurate determinations of photoelastic coefficient at excitonic resonances.

7. DBR-based GaAs/AlAs optomechanical resonators

We use Eq. (2) to calculate the optomechanical coupling factor $g_{om}^{ph} = \frac{\Delta R}{\frac{dR}{d\omega}\Delta\alpha}$. We emphasize that all required parameters needed to determine the purely mechanical contribution are experimentally accessible (dielectric functions), or set by design (the cavity structure). The photoelastic term, on the other hand, can be evaluated taking into account the above discussion related to the photoelastic constant in GaAs close to the exciton resonance. To calculate ΔR well established standard values are used for the dielectric constants of the AlGaAs materials. As a conservative estimation of the photoelastic constants of GaAs close to resonance we use a value of 200. $\frac{dR}{d\omega}$ is calculated for the probe tuned to the flank of the optical cavity mode using the nominal structure. α is the displacement associated to the 20 GHz mode. We calculate using $p_{12} = 200$ that $g_{om}^{ph} = 83$ THz/nm for the photoelastic term, and $g_{om}^{if} = 3.6$ THz/nm for the contribution due to the displacement of spacer and DBR interfaces. A related quantity that is also used to describe the optomechanical coupling is the effective coupling length $L_{om} = (\frac{1}{\omega}\frac{d\omega}{d\alpha})^{-1}$. L_{om} is the length over which a photon's momentum is transferred into the mechanical mode as it propagates in the structure. [55] For the described planar cavity we obtain $L_{om} \sim 600$ or 30 nm, that is, 5 or 0.25 times the spacer thickness, depending on whether the pure mechanical or photoelastic contributions are considered. These values can be compared to several microns for planar Si optomechanical crystals operating in the infrared and at few GHz mechanical frequencies [55]. Nominal Q-factors were used in these estimations. A discussion on the actual cavity Q-factors attainable in these planar DBR-based cavities and at such high vibrational frequencies, is however required. The cavity-mode lifetime is determined by the mirror reflectivity which is set by design. For the reported sample the nominal quality-factors are $Q_{op} \sim Q_{ac} \sim 10^3$, corresponding to cavity escape lifetimes of ~1 ps and ~60 ns for photons and phonons, respectively (the difference arising only from the contrasting speeds of light and sound). The optical cavity finesse can be easily measured experimentally through photoluminescence or reflectivity experiments. Below the GaAs fundamental gap, were light absorption is small, the nominal value coincides excellently well with the experiment. Q-factors in the range of 10^5 have been attained with no fundamental difficulties [100]. Phonons are, however, intrinsically anharmonic. This implies that anharmonic decay must be considered as a possible additional source of lifetime limitation. From picosecond acoustic studies of 60 GHz phonon in GaAs, one can estimate the anharmonic decay lifetime of the 20 GHz first confined mode to be somewhere between 3 and 30 ns [101]. Since we do not observe any significant decay within the measured 3 ns time-window, we conclude that the actual lifetime should be closer to the upper limit. In any case, it is clear that anharmonicity may be partially limiting the phonon cavity Q-factor at room temperature. And would definitively limit it if Q-factors larger than 10^3 would be sought. However, below 80 K anharmonic decay should be negligible [101]. We also note that roughness limitations to the phonon lifetime in MBE-grown structures at these wavelengths are not expected to be critical [25]. Optomechanical phenomena of a dynamical nature arise when the decay time of the photons inside the cavity is comparable to or longer than the mechanical oscillator period [102]. For the studied structure the latter vary between 50 and 10 ps (for the 20 and 100 GHz modes, respectively). It thus turns out that both fully static and purely dynamical regimes should be both attainable with DBR-based cavities in which the cavity photon lifetime can span the range between 1 and 100 ps (Q_{opt} from 10^3 to 10^5).

8. Discussion and conclusions

To summarize, we have shown that hypersound devices formed by ~100 nanometric layers can be conceived for the simultaneous manipulation of light and ultrahigh frequency acoustic vibrations. The performance of this devices is highly predictable, and the available growth techniques, and optimization and design algorithms open new possibilities in the fast developing nanophononics and phonon engineering research. With highly promising results for future nanophononics applications, these devices were able to confine a specific frequency with high quality factors, while at the same time confining light in the VIS–NIR region.

Acknowledgments

The authors acknowledge B. Perrin, G. Rozas, M.F. Pascual Winter, A. Bruchhausen, A. Lemaitre and V. Thierry-Mieg for enlightening discussions.

References

[1] A. Huynh, N.D. Lanzillotti-Kimura, B. Jusserand, B. Perrin, A. Fainstein, M.F. Pascual Winter, E. Perónne, A. Lemaître, Phys. Rev. Lett. 97 (2006) 115502.
[2] V. Narayanamurti, H.L. Störmer, M.A. Chin, A.C. Gossard, W. Wiegmann, Phys. Rev. Lett. 43 (1979) 2012.
[3] N.D. Lanzillotti-Kimura, A. Fainstein, A. Lemaître, B. Jusserand, Appl. Phys. Lett. 88 (2006) 083113.
[4] N.D. Lanzillotti-Kimura, A. Fainstein, B. Jusserand, O. Mauguin, L. Largeau, A. Lemaître, Phys. Rev. B 76 (2007) 174301.
[5] E.S. Landry, M.I. Hussein, A.J.H. McGaughey, Phys. Rev. B 77 (2008) 184302.
[6] M.I. Hussein, M.A. El-Beltagy, J. Phys.: Conf. Ser. 92 (2008) 012110.
[7] Anne-Christine Hladky-Hennion, Jerome Vasseur, Bahram Djafari-Rouhani, Michel de Billy, Phys. Rev. B 77 (2008) 104304.
[8] E.H. El Boudouti, B. Djafari-Rouhani, A. Akjouj, L. Dobrzynski, Surf. Sci. Rep. 64 (2009) 471.
[9] N.D. Lanzillotti-Kimura, B. Perrin, A. Fainstein, B. Jusserand, A. Lemaître, Appl. Phys. Lett. 96 (2010) 053101.
[10] J. Gazalet, S. Dupont, J.C. Kastelik, Q. Rolland, B. Djafari-Rouhani, Wave Motion 50 (2013) 619.
[11] H. Yokohama, Science 256 (1992) 66.
[12] Y. Yamamoto, R.E. Slusher, Phys. Today 46 (1993) 66.
[13] M.S. Skolnick et al., Semicond. Sci. Technol. 13 (1998) 645.
[14] T. Someya, R. Werner, A. Forchel, M. Catalano, R. Cingolani, Y. Arakawa, Science 285 (1999) 1905.
[15] G. Malpuech, A. Kavokin, Semicond. Sci. Technol. 16 (2001). R1.
[16] A. Dousse, J. Suffczynski, A. Beveratos, O. Krebs, A. Lematre, I. Sagnes, J. Bloch, P. Voisin, P. Senellart, Nature 466 (2010) 217.
[17] E. Wertz, L. Ferrier, D.D. Solnyshkov, R. Johne, D. Sanvitto, A. Lematre, I. Sagnes, R. Grousson, A.V. Kavokin, P. Senellart, G. Malpuech, J. Bloch, Nat. Phys. 6 (2010) 860.
[18] M. Galbiati, L. Ferrier, D. Solnyshkov, D. Tanese, E. Wertz, A. Amo, M. Abbarchi, P. Senellart, I. Sagnes, A. Lemaitre, E. Galopin, G. Malpuech, J. Bloch, Phys. Rev. Lett. 108 (2012) 126403.
[19] E. Wertz, A. Amo, D. Solnyshkov, L. Ferrier, T.C.H. Liew, D. Sanvitto, P. Senellart, I. Sagnes, A. Lemaitre, A.V. Kavokin, G. Malpuech, J. Bloch, Phys. Rev. Lett. 109 (2012) 216404.
[20] H.-S. Nguyen, D. Vishnevsky, M. Sturm, D. Tanese, D. Solnyshkov, E. Galopin, A. Lemaitre, I. Sagnes, A. Amo, G. Malpuech, J. Bloch, Phys. Rev. Lett. 110 (2013) 236601.
[21] C. Sturm, G. Malpuech, A. Amo, D. Solnyshkov, I. Sagnes, A. Lemaitre, E. Galopin, H. Flayac, H.-S. Nguyen, D. Tanese, J. Bloch, Nat. Commun. 5 (2014) 3278.

[22] see also M. Trigo, A. Bruchhausen, A. Fainstein, B. Jusserand, V. Thierry-Mieg, Phys. Rev. Lett. 89 (2002) 227402;
J.M. Worlock, M.L. Roukes, Nature 421 (2003) 802.
[23] P. Lacharmoise, A. Fainstein, B. Jusserand, V. Thierry-Mieg, Appl. Phys. Lett. 84 (2004) 3274.
[24] N.D. Lanzillotti-Kimura, A. Fainstein, B. Jusserand, A. Lematre, Phys. Rev. B 79 (2009) 035404.
[25] G. Rozas, M.F. Pascual Winter, B. Jusserand, A. Fainstein, B. Perrin, E. Semenova, A. Lematre, Phys. Rev. Lett. 102 (2009) 015502.
[26] F. Hudert, A. Bartels, C. Janke, T. Dekorsy, K. Kohler, J. Phys.: Conf. Ser. 92 (2007) 012012.
[27] A. Huynh, B. Perrin, N.D. Lanzillotti-Kimura, B. Jusserand, A. Fainstein, A. Lemaitre, Phys. Rev. B 78 (2008) 233302.
[28] N.D. Lanzillotti-Kimura, A. Fainstein, B. Perrin, B. Jusserand, A. Soukiassian, X.X. Xi, D.G. Schlom, Phys. Rev. Lett. 104 (2010) 187402.
[29] M.F. Pascual-Winter, A. Fainstein, B. Jusserand, B. Perrin, A. Lematre, Phys. Rev. B 85 (2012) 235443.
[30] T. Czerniuk, C. Brueggemann, J. Tepper, S. Brodbeck, C. Schneider, M. Kamp, S. Hoefling, B.A. Glavin, D.R. Yakovlev, A.V. Akimov, M. Bayer, 2014 <http://arxiv.org/abs/1401.4359>.
[31] A. Fainstein, B. Jusserand, Light Scattering Solids IX: Novel Mater. Tech. 108 (2007) 17.
[32] A. Fainstein et al., Phys. Rev. Lett. 75 (1995) 3764.
[33] A. Fainstein et al., Phys. Rev. B 53 (1996) R13287.
[34] A. Fainstein, B. Jusserand, Phys. Rev. B 57 (1998) 2402.
[35] N.D. Lanzillotti-Kimura, A. Fainstein, A. Huynh, B. Perrin, B. Jusserand, A. Miard, A. Lematre, Phys. Rev. Lett. 99 (2007) 217405.
[36] N.D. Lanzillotti-Kimura, A. Fainstein, A. Lemaitre, B. Jusserand, B. Perrin, Phys. Rev. B 84 (2011) 115453.
[37] N.D. Lanzillotti-Kimura, A. Fainstein, B. Perrin, B. Jusserand, L. Largeau, O. Mauguin, A. Lemaitre, Phys. Rev. B 83 (2011) 201103.
[38] A. Fainstein, B. Jusserand, V. Thierry-Mieg, Phys. Rev. Lett. 78 (1997) 1576.
[39] Y. Li, Q. Miao, A.V. Nurmikko, H.J. Maris, J. Appl. Phys. 105 (2009) 083516.
[40] N.D. Lanzillotti-Kimura, A. Fainstein, B. Perrin, B. Jusserand, Phys. Rev. B 84 (2011) 064307.
[41] M.M. de Lima Jr., R. Hey, P.V. Santos, A. Cantarero, Phys. Rev. Lett. 94 (2005) 126805.
[42] Mauricio M. de Lima Jr., Paulo V. Santos, Rep. Prog. Phys. 68 (2005) 1639.
[43] M.M. de Lima Jr., M. van der Poel, P.V. Santos, J.M. Hvam, Phys. Rev. Lett. 97 (2006) 045501.
[44] A.V. Scherbakov, T. Berstermann, A.V. Akimov, D.R. Yakovlev, G. Beaudoin, D. Bajoni, I. Sagnes, J. Bloch, M. Bayer, Phys. Rev. B 78 (2008) 241302(R).
[45] T. Berstermann, C. Bruggemann, M. Bombeck, A.V. Akimov, D.R. Yakovlev, C. Kruse, D. Hommel, M. Bayer, Phys. Rev. B 81 (2010) 085316.
[46] E.A. Cerda-Mndez, D.N. Krizhanovskii, M. Wouters, R. Bradley, K. Biermann, K. Guda, R. Hey, P.V. Santos, D. Sarkar, M.S. Skolnick, Phys. Rev. Lett. 105 (2010) 116402.
[47] Edgar A. Cerda-Mendez, Dmitry N. Krizhanovskii, Klaus Biermann, Rudolf Hey, Maurice S. Skolnick, Paulo V. Santos, Phys. Rev. B 86 (2012) 100301(R).
[48] T. Berstermann, C. Bruggemann, A.V. Akimov, M. Bombeck, D.R. Yakovlev, N.A. Gippius, A.V. Scherbakov, I. Sagnes, J. Bloch, M. Bayer, Phys. Rev. B 86 (2012) 195306.
[49] C. Bruggemann, A.V. Akimov, A.V. Scherbakov, M. Bombeck, C. Schneider, S. Hofling, A. Forchel, D.R. Yakovlev, M. Bayer, Nat. Photonics 6 (2012) 30.
[50] P.D. Batista, B. Drescher, W. Seidel, J. Rudolph, S. Jiao, P.V. Santos, Appl. Phys. Lett. 92 (2008) 133502.
[51] M. Maldovan, E.L. Thomas, Appl. Phys. Lett. 88 (2006) 251907.
[52] M. Maldovan, E.L. Thomas, Appl. Phys. B 83 (2006) 595.
[53] A.V. Akimov, Y. Tanaka, A.B. Pevtsov, S.F. Kaplan, V.G. Golubev, S. Tamura, D.R. Yakovlev, M. Bayer, Phys. Rev. Lett. 101 (2008) 033902.
[54] S. Sadat-Saleh, S. Benchabane, F.I. Baida, M.P. Bernal, V. Laude, J. Appl. Phys. 106 (2009) 074912.
[55] M. Eichenfield, J. Chan, R.M. Camacho, K.J. Vahala, O. Painter, Nature 462 (2009) 78.
[56] Y. Pennec, B. Djafari Rouhani, E.H. El Boudouti, C. Li, Y. El Hassouani, J.O. Vasseur, N. Papanikolaou, S. Benchabane, V. Laude, A. Martinez, Opt. Exp. 18 (2010) 14301.
[57] I.E. Psarobas, N. Papanikolaou, N. Stefanou, B. Djafari-Rouhani, B. Bonello, V. Laude, Phys. Rev. B 82 (2010) 174303.
[58] J. Cuffe, D. Dudek, N. Kehagias, P.-O. Chapuis, V. Reboud, F. Alsina, J.G. McInerney, C.M. Sotomayor Torres, Microelectron. Eng. 88 (2011) 2233.
[59] Martin Maldovan, Nature 503 (2013) 209.
[60] A.H. Safavi-Naeini, J.T. Hill, S. Meenehan, J. Chan, S. Groblacher, O. Painter, Phys. Rev. Lett. 112 (2014) 153603.
[61] A. Fainstein, N.D. Lanzillotti-Kimura, B. Jusserand, B. Perrin, Phys. Rev. Lett. 110 (2013) 037403.
[62] K. Vahala, M. Hermann, S. Knuzn, V. Batteiger, G. Saathoff, T.W. Hansch, Th. Udem, Nat. Phys. 5 (2009) 682.
[63] I.S. Grudinin, H. Lee, O. Painter, K.J. Vahala, Phys. Rev. Lett. 104 (2010) 083901.
[64] V.B. Braginsky, S.E. Strygin, S.E. Vyatchanin, Phys. Lett. A 287 (2001) 331.
[65] R.P. Beardsley, A.V. Akimov, M. Henini, A.J. Kent, Phys. Rev. Lett. 104 (2010) 085501.
[66] W. Maryam, A.V. Akimov, R.P. Campion, A.J. Kent, Nat. Commun. 4 (2013) 3184, http://dx.doi.org/10.1038/ncomms.
[67] P.T. Rakich, P. Davids, Z. Wang, Opt. Exp. 18 (2010) 14439.
[68] C. Thomsen, H.T. Grahn, H.J. Maris, J. Tauc, Phys. Rev. B 34 (1986) 4129.
[69] M.F. Pascual Winter, A. Fainstein, B. Jusserand, B. Perrin, A. Lematre, Appl. Phys. Lett. 94 (2009) 103103.
[70] P. Babilotte, P. Ruello, D. Mounier, T. Pezeril, G. Vaudel, M. Edely, J-M. Breteau, V. Gusev, K. Blary, Phys. Rev. B 81 (2010) 245207.
[71] P. Ruello, S. Zhang, P. Laffez, B. Perrin, V. Gusev, Phys. Rev. B 79 (2009) 094303.
[72] B. Perrin, B. Bonello, J.-C. Jeannet, E. Romatet, Phys. (Amsterdam) 219B–220B (1996) 681.
[73] O. Matsuda, I. Ishii, T. Fukui, J.J. Baumberg, O.B. Wright, Physica B 316–317 (2002) 205.
[74] J.-Y. Duquesne, B. Perrin, Phys. Rev. B 68 (2003) 134205.
[75] Emmanuel Peronne, Bernard Perrin, Ultrasonics 44 (2006) 1203.
[76] Florian Hudert, Axel Bruchhausen, Daniel Issenmann, Olivier Schecker, Reimar Waitz, Artur Erbe, Elke Scheer, Thomas Dekorsy, Adnen Mlayah, Jean-Roch Huntzinger, Phys. Rev. B 79 (2009) 201307(R).
[77] Martin Grossmann, Matthias Klingele, Patricia Scheel, Oliver Ristow, Mike Hettich, Chuan He, Reimar Waitz, Martin Schubert, Axel Bruchhausen, Vitalyi Gusev, Elke Scheer, Thomas Dekorsy, Phys. Rev. B 88 (2013) 205202.
[78] Kohji Mizoguchi, Kei Matsutani, Shin-ichi Nakashima, Thomas Dekorsy, Heinrich Kurz, Masaaki Nakayama, Phys. Rev. B 55 (1997) 9336.
[79] A. Bartels, T. Dekorsy, H. Kurz, K. Kohler, Appl. Phys. Lett. 72 (1998) 2844–2846.
[80] Chi-Kuang Sun, Yue-Kai Huang, Jian-Chin Liang, Amber Abare, Steven P. DenBaars, Appl. Phys. Lett. 78 (2001) 1201.
[81] Umit Ozgur, Chang-Won Lee, Henry O. Everitt, Phys. Rev. Lett. 86 (2001) 5604.
[82] Gia-Wei Chern, Kung-Hsuan Lin, Yue-Kai Huang, Chi-Kuang Sun, Phys. Rev. B 67 (2003) 121303(R).
[83] A. Arbouet, N. Del Fatti, F. Vallee, J. Chem. Phys. 124 (2006) 144701–1447014.
[84] D.H. Hurley, R. Lewis, O.B. Wright, O. Matsuda, Appl. Phys. Lett. 93 (2008) 113101.
[85] A. Bruchhausen, R. Gebs, F. Hudert, D. Issenmann, G. Klatt, A. Bartels, O. Schecker, R. Waitz, A. Erbe, E. Scheer, J.-R. Huntzinger, A. Mlayah, T. Dekorsy, Phys. Rev. Lett. 106 (2011) 077401.
[86] Q. Li, K. Hoogeboom-Pot, D. Nardi, M.M. Murnane, H.C. Kapteyn, M.E. Siemens, E.H. Anderson, O. Hellwig, E. Dobisz, B. Gurney, R. Yang, K.A. Nelson, Phys. Rev. B 85 (2012) 195431.
[87] Huarui Sun, Vladimir A. Stoica, Max Shtein, Roy Clarke, Kevin P. Pipe, Phys. Rev. Lett. 110 (2013) 086109.
[88] M.F. Pascual Winter, G. Rozas, A. Fainstein, B. Jusserand, B. Perrin, A. Huynh, P.O. Vaccaro, S. Saravanan, Phys. Rev. Lett 98 (2007) 265501.
[89] A. Fainstein, B. Jusserand, P. Senellart, J. Bloch, V. Thierry-Mieg, R. Planel, Phys. Rev. B 62 (2000) 8199.
[90] R.P. Stanley, R. Houdre, U. Oesterle, M. Ilegems, C. Weisbuch, Phys. Rev. A 48 (1993) 2246.
[91] M. Cardona, in: Light Scattering II, Springer, Berlin, Heidelberg, New York, 1982, p. 19.
[92] B. Jusserand, A. Fainstein, R. Ferreira, S. Majrab, A. Lemaitre, Phys. Rev. B 85 (2012) R041302.
[93] A. Feldman, D. Horowitz, J. Appl. Phys. 39 (1968) 5597.
[94] P. Renosi, J. Sapriel, Ultrasonics 31 (1993) 327.
[95] P. Etchegoin et al., Phys. Rev. B 46 (1992) 15139.
[96] Z.V. Popovic et al., Phys. Rev. B 48 (1993) 1659.
[97] P. Etchegoin, A. Fainstein, A.A. Sirenko, L.C. Lew Yan Voon, P. Santos, M. Cardona, K. Totenmeyer, K. Eberl, Phys. Rev. B 53 (1996) 13662.
[98] D. Papadimitriou, W. Richter, Phys. Rev. B 72 (2005) 075212.
[99] J.L. Yu, Y.H. Chen, X. Bo, C.Y. Jiang, X.L. Ye, S.J. Wu, H.S. Gao, J. Appl. Phys. 113 (2013) 083504.
[100] V. Loo, L. Lanco, A. Lemaitre, I. Sagnes, O. Krebs, P. Voisin, P. Senellart, Appl. Phys. Lett. 97 (2010) 241110.
[101] W. Chen, H.J. Maris, Z.R. Wasilewski, Philos. Mag. Part B 70 (1994) 687.
[102] T.J. Kippenberg, K.J. Vahala, Science 321 (2008) 1172.